

RSC Advances



This is an *Accepted Manuscript*, which has been through the Royal Society of Chemistry peer review process and has been accepted for publication.

Accepted Manuscripts are published online shortly after acceptance, before technical editing, formatting and proof reading. Using this free service, authors can make their results available to the community, in citable form, before we publish the edited article. This *Accepted Manuscript* will be replaced by the edited, formatted and paginated article as soon as this is available.

You can find more information about *Accepted Manuscripts* in the [Information for Authors](#).

Please note that technical editing may introduce minor changes to the text and/or graphics, which may alter content. The journal's standard [Terms & Conditions](#) and the [Ethical guidelines](#) still apply. In no event shall the Royal Society of Chemistry be held responsible for any errors or omissions in this *Accepted Manuscript* or any consequences arising from the use of any information it contains.



Journal Name

ARTICLE

A surfactant-assisted high energy ball milling technique to produce colloidal nanoparticles and nanocrystalline flakes in Mn-Al alloys

Received 00th January 20xx,
Accepted 00th January 20xx

DOI: 10.1039/x0xx00000x

www.rsc.org/

P. Saravanan,^{*a} D. Deepika,^a Jen-Hwa Hsu,^{*b} V.T.P. Vinod,^c Miroslav Černík^c and S.V. Kamat^a

We herein exploit the advantages of surfactant assisted-high energy ball milling (SA-HEBM) for the processing of Mn-Al alloy. In this method, a combination of two surfactants such as oleic acid and oleylamine was used along with a solvent *n*-heptane during milling. The use of SA-HEBM process yielded two different products: a sediment powder consisting of sub-micron sized Mn-Al flakes and a suspension in the milling medium (colloid) containing Mn-Al nanoparticles. The colloid consisted of Mn-Al nanocrystalline particles (5–16 nm) having lamellar morphology with average thickness of 1.5 nm and length of 16 nm. Magnetic measurements on these colloidal nanoparticles demonstrated almost a non-magnetic behavior at 300 K. The Mn-Al sediment powders obtained with the SA-HEBM process at regular intervals of milling time were investigated for their structural and magnetic performance and also compared with the corresponding powders obtained from the conventional HEBM process. The phase composition of Mn-Al powders processed by both HEBM and SA-HEBM is quite similar and they adhere to the phase constituents of parent alloy: τ -, β -phases with some traces of ϵ -phase. Nevertheless, the estimated magnetic parameters such as saturation magnetization and coercivity for the SA-HEBM powders exhibited improved values, as compared to the HEBM powders. A maximum coercivity of 4.88 kOe was obtained for the 8-h milled SA-HEBM powder and this value is 23 % higher than that of HEBM processed powder. The results were explained based on the effect of surfactants on the morphology of the milled powder.

1. Introduction

In recent years, increasing global attention has been directed towards the development of rare earth (RE) free permanent magnetic (PM) materials. This is mainly driven by the increasing cost and decreasing reserves of RE resources as well as the near monopolistic control of these resources by China.^{1–4} Among RE-free PMs, near-equiatomic Mn-Al and structurally stabilized Mn-Al-C alloys have shown the most promise because of their superior magnetic properties as compared to the conventional hard ferrites, Alnicos and Fe-Cr-Co alloys.^{5–8} The superior ferromagnetic properties in Mn-Al alloys are attributed to the τ -phase, which has a composition range of 42–49 at. % Al. The τ -MnAl is an intermetallic phase with a face centred tetragonal structure ($L1_0$) wherein the Mn atoms occupy the (0, 0, 0) and (1/2, 1/2, 0) sites while the Al atoms occupy the (0, 1/2, 1/2) sites. For slightly Mn rich compositions, not all the Mn atoms can occupy the (0, 0, 0) and (1/2, 1/2, 0) sites and the excess Mn atoms are accommodated on

the (0, 1/2, 1/2) sites wherein they share with the Al atoms. This deviation from the ideal site occupancy results in an antiferromagnetic coupling between the Mn atoms occupying these different sites and causes an enhancement in the magnetization.⁹ The τ -Mn-Al phase exhibits interesting hard magnetic properties, viz., coercivity (H_c) of 1.5–4.0 kOe, saturation magnetization (M_s) of 88–98 emu/g, Curie temperature (T_c) of 650 K and maximum energy product values of 2–7 MGOe [9, 10]. However, in the Mn-Al phase diagram, the τ -MnAl is formed in the two-phase region of γ_2 and β -Mn and hence, it is very difficult experimentally to obtain 100% τ -MnAl phase in near equiatomic Mn-Al alloys.¹¹ The commonly adopted strategy for obtaining \sim 100% τ -phase in near equiatomic Mn-Al alloys is by rapid quenching of the high-temperature non-magnetic ϵ -phase followed by isothermal annealing at temperatures between 673 and 973 K for short duration, or by cooling at a rate of 10 K/min from the high-temperature ϵ -phase region.^{12–14} Carbon-doped MnAl has been found to be structurally more stable and to show improved magnetic and mechanical properties, although it has a lower T_c than the undoped alloys.^{13–17}

Over the past several years, extensive efforts have been made on the fabrication of τ -MnAl alloys by adopting non-equilibrium processing techniques such as melt spinning,^{15,16} splat quenching,¹⁷ gas atomization,¹⁸ plasma arc discharge¹⁹ and mechanical milling.^{10,11} Among all these techniques, mechanical milling is the most popular. This is because; this method is relatively simple,

^a Defence Metallurgical Research Laboratory, Hyderabad-500058, India. E-mail: psdrdo@gmail.com; ps@dmrl.drdo.in

^b Department of Physics, National Taiwan University, Taipei 106, Taiwan, E-mail: jhhsu@phys.ntu.edu.tw.

^c Institute for Nanomaterials, Advanced Technologies and Innovation, Department of Natural Sciences, Technical University of Liberec, Liberec 1, Studentská 1402/2, 46117, Czech Republic.

inexpensive and efficient in producing Mn-Al nanocrystalline powders in bulk amount. A brief summary of the magnetic properties achieved *via* mechanical milling of Mn-Al and Mn-Al-C alloys is presented in Table 1.^{10,11,15,16,20-29} Despite the fact that mechanical milling has been widely employed in the processing of Mn-Al alloys, the realization of maximum achievable hard magnetic properties (close to the theoretical limits) in the bulk form of Mn-Al magnets still poses several challenges. This is mainly because of the issues such as polydispersity, particle contamination, agglomeration, oxidation and reduced anisotropy encountered in the conventional milling process. A method increasingly being adopted to improve the performance of mechanically milled magnetic powders in other systems is by adding surfactants during the milling process. In fact, in the recent past, the use of surfactants during high-energy ball milling (HEBM) has become commonplace and is referred to as surfactant assisted-HEBM.³⁰⁻³⁸ The use of surfactants during milling provides a capping layer on the freshly cleaved surface of the particles, which reduces the cold-welding between the particles. As a result, fine particles with narrow size distribution and shape homogeneity are produced by the SA-HEBM process.³³⁻³⁶ In addition, it has been demonstrated that by choosing appropriate powder/surfactant ratio, interesting structure/morphology and magnetic properties can be achieved in the milled powders. One such feature is 'flaking', which is observed not only in the case of malleable metals and alloys, viz., Fe, Co, Ni, Cu, Fe-Co, Fe-Co-Zr, Fe-Si-Al and Sn-Ag-Cu,³⁹⁻⁴² but also in inherently brittle materials such as RE intermetallic compounds: Nd-Fe-B, SmCo₅, Tb-Dy-Fe, PrCo₅, CeCo₅ and NdCo₅.³⁰⁻³⁸ The nanoflakes produced by the SA-HEBM process, tend to show excellent texture, anisotropy and magnetic properties and these properties are highly beneficial for fabricating anisotropic PMs.^{30-38,43} However, to the best of our knowledge, so far no detailed investigation has been carried out on the processing of Mn-Al powders using SA-HEBM technique. These studies are especially necessary and important for realizing the full potential of Mn-Al alloys as high performance RE-free PMs.

In light of the above, the objective of this study was to systematically investigate the effect of SA-HEBM process on the structure, microstructure, morphology and magnetic behaviour of the Mn₅₄Al₄₆ alloy using a combination of two surfactants such as oleic acid and oleylamine.

2. Experimental

Mn₅₆Al₄₄ alloy was arc-melted using high purity (>99.5%) constituent elements Mn and Al in appropriate amounts under argon atmosphere and the melting was repeated at least three times to attain compositional homogeneity. An excess amount of Mn (2 wt. %) was added to compensate for the evaporation losses that occur during melting. The compositional analysis of Mn-Al alloy ingots was performed using chemical analysis as well as energy dispersive spectroscopy (EDS) in a scanning electron microscope (SEM). Prior to the milling process, the alloy ingots were crushed down to a particle size of < 300 μm. High energy ball milling was performed in a planetary ball mill (FRITSCH pulverisette) using tungsten carbide milling vial and balls. In the milling process, *n*-heptane (99.8 % purity) was used as a solvent, while 99 % purity oleic acid (OA) and oleylamine (OY) were used as surfactants. A ratio close to 1:1 (in wt. %) was maintained for the two surfactants,

while the total amount of surfactant used was ~ 10 – 12 wt. % of the starting powder. The milling was carried out at a constant speed of 200 rpm with ball to powder ratio of 10:1 (in terms of weight) and the milling time was varied from 2 to 10 h. In order to understand the actual role of surfactants on the structural and magnetic properties of Mn-Al alloy, HEBM was also carried out in the absence of surfactants with the other milling parameters unaltered. For the samples milled without surfactant, the colour of the solvent (heptane) did not change and the milled ingredients sedimented at the bottom of the milling vial. In contrast, the use of surfactants (OA+OY) during milling resulted in a ultrafine particle suspension (referred to as colloid) along with coarse particles (referred to as powder) sedimented at the bottom of the milling vial (Fig. 1). The presence of surfactant is thus able to separate out the extremely fine-size particles from the sediment.

Small angle X-ray scattering (SAXS) measurements for the Mn-Al colloidal samples were carried out in a transmission geometry using Cu-K_α radiation ($\lambda = 0.154$ nm) from a sealed long fine focus X-ray tube powered by a high-voltage X-ray generator PW3830 operated at 40 kV and 50 mA. The acquired scattering data were used to calculate the size, shape and distribution of the Mn-Al particles in the colloid. Data were obtained in the form of scattered X-ray intensity '*I*' as a function of the scattering vector, $q = (4\pi/\lambda) \sin\vartheta$ [1/nm], where ϑ is the scattering angle and λ is the wavelength of the radiation.⁴⁴ The data analysis was performed using GIFT software. Morphology of the Mn-Al colloid and the sedimented powders were also characterized using a transmission electron microscopy (TEM) equipped with energy dispersive X-ray spectroscopic analysis (EDS) facility. For the colloid, TEM specimens were prepared by placing a drop of colloid on a Formvar carbon-coated copper TEM grid, which was then kept overnight in a dessicator for drying; while for the sediment powders, TEM specimens were prepared by dimpling and ion milling in Gatan make Dual Ion Mill (Model 600) at 5 kV. The evolution of powder morphology and the identification of phases formed in the sediment powders were studied using scanning electron microscopy (SEM, Leo 440i) and X-ray diffraction (Philips, Cu-K_α radiation), respectively. Thermo-gravimetric (TG) studies were performed by differential scanning calorimetry (DSC, LABSYS EVO, SETARAM Instrumentation, Caluire, France) at a temperature ramp rate of 15 K/min up to 1273 K under nitrogen atmosphere. Magnetic properties of the colloid, as well as powder samples were evaluated using a superconducting quantum interference device (SQUID)-vibrating sample magnetometer (VSM) up to a maximum field of 70 kOe (7 T).

3. Results and discussion

3.1 Microstructure and magnetic properties of as-cast Mn-Al alloy

The microstructure and composition of the Mn-Al alloy ingot obtained by arc-melting is presented in Figs. 2a and b, respectively. Predominantly a two-phase microstructure is observed in the Mn-Al alloy ingot and the EDS line scan profile indicates that the Mn concentration drastically decreases at a distance of 20 nm on each side of the interface between the two phases. The two phases were identified as τ -MnAl and β -Mn (Mn-rich) phases from the XRD pattern of the as-cast alloy (Fig. 3a). The XRD pattern also showed the presence of γ_2 and ε -phases but their volume fractions are not significant. Based on the relative intensities of the main peaks

present in the as-cast alloy ingot, the relative phase contents are estimated to be 68, 23 and 9 at.% for τ - and β - and other phases, respectively. In Fig. 3b, we show the cumulative EDS analysis of the Mn-Al alloy revealing the presence of only Mn and Al, with no other impurities. The estimated elemental composition was also in close agreement with the targeted $\text{Mn}_{54}\text{Al}_{46}$ composition and this was further confirmed by chemical analysis.

Prior to subjecting the as-cast Mn-Al alloy ingot for milling, it is important to know its magnetic parameters such as M_s , H_c and T_c . The magnetic hysteresis loop obtained at room temperature (RT) for the as-cast Mn-Al alloy is shown in Fig. 4a. It can be noticed that the $M-H$ curve is not saturated even at 40 kOe (4 T). This could be probably due to the presence of two components: a ferromagnetic τ -phase contributing magnetic saturation and other paramagnetic or antiferromagnetic phases such as β , γ_2 and ε -phases giving a linear contribution at high field. Such a conclusion is drawn based on the phase composition ascertained by XRD (Fig. 3a). From the $M-H$ loop, $M_{s,4T}$ of 67 emu/g and H_c of 1.28 kOe were estimated. Since the τ -phase is the only known ferromagnetic phase in the Mn-Al alloy system, the M_s of the alloy should be proportional to the amount of τ -phase present in the alloy. Thus the weight fraction of τ -phase in the Mn-Al alloy can be estimated from the measured M_s value. A simple calculation (based on rule of mixtures) assuming M_s value of 92 emu/g for τ -Mn-Al^{10,45} suggests that the obtained M_s value corresponds to ~ 72 wt. % of τ -phase in the as-cast Mn-Al alloy and this value is in agreement with the phase composition estimated by XRD. The thermo-magnetic ($M-T$) measurements for the as-cast Mn-Al alloys were performed using a high-temperature vibrating sample magnetometer under an applied field of 200 Oe and the results are plotted in Fig. 4b. It can be seen that the $M-T$ curve shows a sharp transition temperature at ~ 638 K. This value is slightly less than the T_c value (655 K), experimentally obtained by Zeng *et al.* for the τ -phase.¹² The lower T_c value obtained in the present study can be attributed to the presence of other non-magnetic phases in the as-cast alloy.^{16,46}

3.2 Morphology and magnetic properties of SA-HEBM processed Mn-Al colloid

The structural and magnetic properties of the colloid from the 8-h SA-HEBM processed samples were studied in detail. This is because the colloid produced after 8-h of milling had a high particle density, as discerned by the colour of the colloid (black). The TEM micrograph of Mn-Al colloids produced by the SA-HEBM process after 8-h of milling is shown in Fig. 5a. A highly irregular morphology with particle sizes ranging from 5 to 16 nm is observed. The EDS analysis confirmed the presence of Mn and Al in these fine particles and the selected area electron diffraction (SAED) pattern for one of the particles shown in Fig. 5b reveals the crystalline nature of the Mn-Al nanoparticles.

The TEM observations on the morphology and size of Mn-Al nanoparticles created during the SA-HEBM process are further corroborated by the results of SAXS. In fact the SAXS results are much more representative than the TEM results as a significantly larger number of particles are sampled. In the present study, SAXS technique was applied to investigate the size, shape and distribution of Mn-Al nanoparticles from the scattering data by means of the well-established 'indirect Fourier transformation' method followed by the numerical deconvolution of the pair

distance distribution function (PDDF).⁴⁶ The experimental scattering function $I(q)$ versus scattering vector ($\log(q)$) obtained for the Mn-Al colloidal sample is shown in Fig. 6a. A Power law can be easily fit to this variation which clearly indicates that the shape of the particles is mostly lamellar.⁴⁷ The pair distance distribution function, $p(r)$, of the particles was obtained from the generalized indirect Fourier transformation of the scattering function: $p(r) = (1/2\pi^2 A) \int q^2 I(q) \cos(qr) dq$, where $p(r)$ is the PDDF along a direction perpendicular to the lamellar surface, r is a real space distance (units of nm), q is the scattering vector ($0 - \infty$), A is the area of lamella and $I(q)$ is the experimental scattering function. The $p(r)$ curve of Mn-Al colloidal sample shown in Fig. 6b confirms that the Mn-Al nanoparticles are mostly lamellar. A thickness of about 1.5 nm and a length of 16 nm were estimated for the Mn-Al nanoparticles. The plasticity of inherently brittle materials is known to increase dramatically in the nanocrystalline regime because of activation of deformation mechanisms such as grain boundary sliding^{48,49} and this can explain the formation of lamellar particles.

The magnetic properties of SA-HEBM processed Mn-Al nanoparticles were investigated by SQUID-VSM. Fig. 7 shows the applied magnetic-field dependence of the magnetization values measured at two temperatures viz., 300 and 5 K. The magnetization values do not saturate even at 70 kOe at both the temperatures. At 5 K, a linear curve corresponding to a typical paramagnetic behaviour is evidenced. In contrast, a distinct hysteresis curve with a superposition of super-paramagnetic and paramagnetic components can be discerned. This unusual behavior is probably due to the two phases present in the Mn-Al colloids: (i) a τ -MnAl phase with particle sizes lower than the critical size (superparamagnetic) and (ii) a β -Mn phase with paramagnetic nature.^{50,51} However, a more detailed study on the Mn-Al colloidal samples is essential to ascertain the above fact.

3.3 Structural and magnetic properties of sedimented Mn-Al powders processed by HEBM and SA-HEBM

The actual surfactant content present in the SA-HEBM Mn-Al powder and the phase changes that occur during the thermal treatment were investigated by TG/DSC. The TG curve for 8-h milled SA-HEBM Mn-Al powders showed a two-step weight-decline pattern with inflections at ~ 658 and ~ 741 K (Fig. 8) which correspond to the degradation of surfactants: OA and OY, respectively. A weight loss of ~ 17 % was estimated which suggests that SA-HEBM processed powders contain about 17 wt.% surfactants after 8-h of milling.

A typical SEM micrograph of as-cast Mn-Al alloy after crushing is shown in Fig. 9. It can be seen that the crushed powder shows angular and irregular shape particles with sizes in the range of 1 - 40 μm . The evolution of particle morphology and size as a function of milling time for the Mn-Al powders processed without and with OA+OY is depicted in Fig. 10. In the case of Mn-Al powders without OA+OY, a distinct transformation from irregular/angular shape of the starting Mn-Al powder into small aggregates can be noticed with progressive milling (Figs. 10a-d). Two opposite mechanisms are operative in a HEBM process.³¹ On one hand, the particles break as a result of the internal strain created by the high pressure exerted on the particles because of the intensive milling action. On the

other hand, the finely divided particles tend to agglomerate to minimize their surface energy.³⁷ The HEBM process proceeds by the successive crushing and coalescence of the particles leading to equiaxed and homogenous particles whose size depends on the nature of the powder and milling conditions. In contrast, the SA-HEBM processed Mn-Al powder shows the gradual development of flake-like morphology with increasing milling time (Figs. 10e-h). In fact, the majority of the particles in the SA-HEBM Mn-Al powder exhibit flaky morphology, within the 4-h of milling (Fig. 10f). The mechanism of flake formation during surfactant assisted milling has been proposed by Cui *et al.* in both SmCo_5 ³¹ and $\text{Nd}_2\text{Fe}_{14}\text{B}$.³⁰ According to them, the irregular particles formed during crushing fail by cleavage along the easy glide basal plane without an appreciable increase in the density of crystal defects. This is followed by continuation of cleavage along parallel basal planes *via* layer-by-layer peeling or splitting to form sub-micron thick flakes. The presence of OA+OY during milling causes these flakes to be coated by the surfactant which prevents their cold welding and hence their agglomeration, resulting in flake-like morphology. A similar mechanism is operative in Mn-Al alloy, as evidenced by the SEM micrograph of 2-h SA-HEBM powder (Fig. 11). The dimensions of the Mn-Al flakes were estimated as a function of milling time using the SEM micrographs and the results are summarized in Table 2. The thickness of flakes is in the range of 50 – 3000 nm while their length varies from 1–90 μm . Upon increasing the milling time, the flakes become increasingly thinner and longer. Flakes with aspect ratio as high as 10^2 to 10^3 are observed in the case of 8 h milled SA-HEBM powder.

Representative TEM microstructure of a Mn-Al flake processed by SA-HEBM for 8 h and the corresponding SAED pattern are shown in Figs. 12a and b, respectively. These figures reveal the co-existence of multiple grains with two distinct phases: τ -MnAl (tetragonal structure, JCPDS card No.40-1150) and β -Mn (complex cubic structure, JCPDS 03-1177). The estimated average grain size values for the 8-h SA-HEBM processed Mn-Al flakes are in the range of 13–20 nm. These grain size values are consistent with the grain sizes calculated from the XRD patterns using the Scherrer's formula. The grain size values for different milling times with and without OA+OY are given in Table 2. In both the cases, the calculated grain-size values are found to decrease with increase of milling time from 0 to 8 h. However, for the powders milled without OA+OY, the grain size values are found to decrease only up to 6-h of milling and beyond that there is no significant change in the grain size values. It can also be observed from Table 2 that the estimated grain size values for the SA-HEBM Mn-Al powder at similar milling intervals are slightly lower than those obtained for the HEBM Mn-Al powder. The XRD patterns for the Mn-Al powders processed without and with OA+OY, as a function of milling time are shown in Figs. 13a and b, respectively. The XRD patterns are almost similar and in both cases, the presence of τ - and β -phases with some traces of ϵ -phase are evident, similar to the parent alloy ingot. In addition, the intensity of τ -phase tends to decrease with increase of milling time, which can be ascribed to the grain-size reduction induced by the HEBM process (Table 2).

The magnetic hysteresis curves of the HEBM and SA-HEBM Mn-Al powders are shown in Figs. 14a and b, respectively. The hysteresis loops of both powder samples demonstrate typical hard

magnetic characteristics with smooth and single-phase magnetization behaviour. With increase in milling duration, the hysteresis loops of HEBM Mn-Al powder tend to show a small kink in the 2nd quadrant (indicated by an arrow in Fig. 14a). This can be attributed to the lack of inter-grain exchange coupling.^{52,53} On the contrary, SA-HEBM Mn-Al powders do not show any kink in the hysteresis loop even after 8-h of milling. This indicates that the coating of surfactants on the Mn-Al particles during the milling process facilitates the inter-grain exchange coupling. The magnetic parameters such as $M_{s,3T}$ and H_c were estimated from the RT temperature hysteresis loops and are plotted against milling time (Fig. 15). In both the cases, the $M_{s,3T}$ values tend to decrease with increase in milling time (Fig. 15a). The loss of magnetization is attributed to the decrease in the fraction of ferromagnetic τ -phase with increasing milling time (Fig. 13). In contrast, the H_c values demonstrated an increasing trend against milling time (Fig. 15b) and this trend can be explained by the dependence of H_c on the τ -MnAl grain size.^{12,13,26} For the HEBM Mn-Al powder, the H_c value attained a maximum value of 3.96 kOe (8 h); while for the powders milled with OA+OY, the H_c value increased to a maximum of 4.88 kOe (8 h). The observed high H_c values in the Mn-Al flakes motivated us to probe the magneto-crystalline anisotropy constant, K_1 of these flakes. Accordingly, K_1 value of 0.84 MJ/m^3 was calculated for the 8-h SA-HEBM processed Mn-Al powders using the equation $K_1 = \mu_0 M_s H_a / 2$, where μ_0 is the permeability of free space and H_a is the anisotropy field.⁵⁰ This value is slightly higher than those processed without OA+OY (0.65 MJ/m^3), as well as with respect to the bulk alloy having similar composition (0.75 MJ/m^3). In addition to the increase in K_1 , the significant grain-size reduction observed in the SA-HEBM powders (Table 2), is an obvious reason for the H_c enhancement.

The magnetic properties of the as-milled Mn-Al powders without and with OA+OY were investigated after being subjected to annealing at 623 K for 10 min. The estimated M_s and H_c values for the annealed powders are shown in Figs. 15c and d, respectively. In both the cases, it is interesting to note that the M_s values tend to increase at the expense of H_c . For the SA-HEBM powders (8-h), the M_s and H_c values: 24.7 emu/g and 4.88 kOe are transformed into 31.9 emu/g and 4.35 kOe, respectively after annealing. Whereas in the case of HEBM powders (8-h), the M_s and H_c values: 18.5 emu/g and 3.96 kOe are changed into 28.2 emu/g and 3.02 kOe, respectively. The above results confirm that the observed decrease in the H_c is somewhat lower in the case of SA-HEBM powders. A possible reason for the H_c retention could be the presence of OA+OY coating, which inhibits the grain-growth caused by annealing.

Further, it is also of particular interest to investigate the H_c values as a function of temperature. For this purpose, 8-h as-milled powder samples were investigated, as they demonstrated higher H_c values. The 2nd quadrant demagnetization curves obtained at different temperatures for the 8-h milled Mn-Al powders without and with OA+OY are shown in Figs. 16a and b, respectively. In both the cases, the H_c values are found to increase gradually with decrease in temperature from 300 to 5 K. As discussed previously, in the case of 8-h milled Mn-Al powders without OA+OY, the demagnetization curve at 300 K contains a shoulder (step), which becomes more pronounced at lower temperatures (dashed line marked in Fig. 16a). The H_c and the fields where the steps appear

were estimated from the demagnetization curves and they are plotted as a function of temperature in the inset of Fig. 16a. Different trends for H_c and the field where the step appears is observed which confirms the existence of hard and soft phases in these powders. The field where the step appears remains in the range of 0.23 – 0.45 kOe; while the H_c values significantly increase with decrease in temperature which confirms the existence of two-phases and lack of inter-grain exchange coupling in the Mn-Al powders milled without OA+OY. The two-phase behavior could be probably attributed to the existence of hard (τ -MnAl) and soft (β -Mn) magnetic components in the 8-h milled HEBM powders (Fig. 13). At this point, it should be mentioned that although β -Mn is mostly considered as a non-magnetic phase; some theoretical studies propose the existence of a marginally ferromagnetic behavior in β -Mn.^{51,53,54}

In contrast, the 8-h milled SA-HEBM powders demonstrate smooth magnetization behaviour with no apparent kink in their demagnetization curves (Fig. 16b), which confirms the existence of strong inter-grain exchange coupling in these samples.^{52,53} With the use of OA+OY during the HEBM process, maximum H_c values of 4.88 and 8.2 kOe were achieved at 300 and 5 K, respectively and these values are about 23 % higher than that of those achieved for the samples processed without OA+OY (inset of Fig. 16). The high H_c values obtained with the SA-HEBM process can also be credited to the surfactant action. The presence of surfactants on the particle surfaces not only imparts strong exchange coupling for the hard/soft magnetic phases; but also traps away the finer particles from the sediment powders.³⁷ It is also worth noting that the H_c values obtained in the present study are significantly higher than those obtained by any other processing techniques. Further, the present approach does not require heat treatment steps for the H_c enhancement of Mn-Al milled powders. This is an additional advantage of SA-HEBM processing of Mn-Al alloys towards PM applications, as without any heat treatment such a high H_c has not been achieved in the mechanically milled Mn-Al powders [Table 1 and cited references therein].

4. Conclusions

- The use of surfactants such as OA and OY during HEBM of Mn-Al alloy resulted in two families of products: a fine particle suspension with non-magnetic nature and sediment powders with interesting hard magnetic properties.
- The OA+OY coated Mn-Al powders revealed the development of high-aspect ratio sub-micron size flakes with nanocrystalline grains, even after 4-h of SA-HEBM process. Upon increasing the milling time, the flakes become increasingly thinner and longer. The thickness of flakes was in the range of 50 – 3000 nm while their length varied from 1–90 μm .
- The 2nd quadrant demagnetization curves for the 8-h SA-HEBM Mn-Al powders demonstrated smooth magnetization behaviour; while the HEBM Mn-Al powders showed a kink in their demagnetization curves.
- Maximum H_c values of 4.88 kOe (300 K) and 8.2 kOe (5 K) were achieved for the 8-h SA-HEBM Mn-Al powder and these values are about 23 % higher than those obtained for the HEBM powder. A noteworthy aspect of the SA-HEBM process is that

these high H_c values were realized without employing any heat treatment.

Acknowledgements

The financial support for the present study was extended by Defence Research and Development Organization (DRDO), Government of India. One of the authors, DD wishes to thank Sri Ramakrishna Engineering College, Coimbatore for granting permission to carry out the project work at DMRL. The authors VTPV and MC acknowledge the support rendered by the Ministry of Education, Youth and Sports under the National Programme for Sustainability I, OPR&DI project (LO1201) and OP VaVpl of the Centre for Nanomaterials, Advanced Technologies and Innovation - CZ.1.05/2.1.00/01.0005.

Notes and references

- 1 P.C. Dent, *J. Appl. Phys.*, 2012, **111**, 07A721-1–07A721-6.
- 2 B. Balamurugan, B. Das, R. Skomski, W.Y. Zhang, D.J. Sellmyer, *Adv. Mater.*, 2013, **25**, 6090-6093.
- 3 R. Skomski, M. Priyanka, P. Kumar, B. Balamurugan, K. Arti, D. Sellmyer, *IEEE Trans. Magn.*, 2013, **49**, 3215-3220.
- 4 L. H. Lewis, F. Jiménez-Villacorta, *Metall. Mater. Trans.*, 2013, **44**, S2-S20.
- 5 A.J.J. Koch, P. Hokkelling, M.G.V.D. Steeg, K.J. De Vos, *J. Appl. Phys.*, 1960, **31**, 75S-77S.
- 6 J.M.D. Coey, *Script. Mater.*, 2012, **67**, 524-529.
- 7 H. Kono, *J. Phys. Soc. Jpn.*, 1958, **13**, 1444-1451.
- 8 J.H. Park, Y.K. Hong, S. Bae, J.J. Lee, J. Jalli, G.S. Abo, N. Neveu, S.G. Kim, C.J. Choi, J.G. Lee, *J. Appl. Phys.*, 2010, **107**, 09A731-1–09A731-3.
- 9 F. Jiménez-Villacorta, J.L. Marion, J.T. Oldham, M. Daniil, M.A. Willard, L.H. Lewis, *Metals*, 2014, **4**, 8-19.
- 10 P.C. Kuo, Y.D. Yao, J.H. Huang, C.H. Chen, *J. Magn. Magn. Mater.*, 1992, **115**, 183-186.
- 11 A. Chaturvedi, R. Yaqub, I. Baker, *J. Phys. Condens. Matter*, 2014, **26**, 064201.
- 12 Q. Zeng, I. Baker, Z-c. Yan, *J. Appl. Phys.*, 2006, **99**, 08E902-1–08E902-3.
- 13 Q. Zeng, I. Baker, J.B. Cui, Z.C. Yan, *J. Magn. Magn. Mater.*, 2007, **308**, 214-226.
- 14 J.Z. Wei, Z.G. Song, Y.B. Yang, S.Q. Liu, H.L. Du, J.Z. Han, D. Zhou, C.S. Wang, Y.C. Yang, A. Franz, D. Tobbens, J.B. Yang, *J. AIP Adv.*, 2014, **4**, 127113-1–127113-11.
- 15 E. Fazakas, L.K. Varga, F. Mazaleyrat, *J. Alloys Compd.*, 2007, **434**, 611-613.
- 16 Z.W. Liu, C. Chen, Z.G. Zheng, B.H. Tan, R.V. Ramanujan, *J. Mater. Sci.*, 2012, **47**, 2333-2338.
- 17 Y.J. Kim, J.H. Perepezko, *J. Appl. Phys.*, 1992, **71**, 676-680.
- 18 J-G. Lee, X-L. Wang, Z-D. Zhang, C-J. Choi, *Thin Solid Films*, 2011, **519**, 8312-8316.
- 19 J-G. Lee, P. Li, C-J. Choi, X-L. Dong, *Thin Solid Films*, 2010, **519**, 81-85.
- 20 D.C. Crew, P.G. McCormick, R. Street, *Script. Metall. Mater.*, 1995, **32**, 315-318.
- 21 M.J. Lucis, T.E. Prost, X. Jiang, M. Wang, J.E. Shield, *Metals*, 2014, **4**, 130-140.
- 22 A. Chaturvedi, R. Yaqub, I. Baker, *Metals*, 2014, **4**, 20-27.
- 23 P. Saravanan, V.T.P. Vinod, M. Černík, D. Chakravarty, P. Ghosal, S.V. Kamat, *Mater. Lett.*, 2014, **137**, 369-372.
- 24 J.H. Huang, P.C. Kuo, C.H. Chen, *J. Mater. Sci.*, 1994, **29**, 4819-4823.

- 25 O. Kohmoto, N. Kageyama, H. Haji, M. Uchida, Y. Matshushima, *J. Phys. Conf. Series*, 2011, **266**, 012016.
- 26 O. Obi, L. Burns, Y. Chen, T. Fitchorov, S. Kim, K. Hsu, D. Heiman, L.H. Lewis, V.G. Harris, *J. Alloys Compd.*, 2014, **582**, 598-602.
- 27 P. Saravanan, V.T.P. Vinod, M. Černík, A. Selvapriya, D. Chakravarty, S.V. Kamat, *J. Magn. Magn. Mater.*, 2015, **374**, 427-432.
- 28 H.X. Wang, P.Z. Si, W. Jiang, X.F. Xiao, J.G. Lee, C.J. Choi, M. Zhong, Z.F. Li, H.L. Ge, *Phys. Sci. Int. Jr.*, 2014, **4**, 536-541.
- 29 O. Obi, L. Burns, Y. Chen, S. Bennett, M. Sawicki, D. Kaplan, A.M. Arango, L.H. Lewis, V.G. Harris, *IEEE Trans. Magn.*, 2013, **49**, 3372-3374.
- 30 B.Z. Cui, L.Y. Zheng, W.F. Li, J.F. Liu, G.C. Hadjipanayis, *Acta Mater.*, 2012, **60**, 1721-1730.
- 31 B.Z. Cui, W.F. Li, G.C. Hadjipanayis, *Acta Mater.*, 2011, **59**, 563-571.
- 32 L. Zheng, B. Cui, G.C. Hadjipanayis, *Acta Mater.*, 2011, **59**, 6772-6782.
- 33 P. Saravanan, R. Gopalan, R. Priya, P. Ghosal, V. Chandrasekaran, *J. Alloys Compd.*, 2009, **477**, 322-327.
- 34 P. Saravanan, M. Premkumar, A.K. Singh, R. Gopalan, V. Chandrasekaran, *J. Alloys Compd.*, 2009, **480**, 645-649.
- 35 L. Zheng, W. Li, B. Cui, G.C. Hadjipanayis, *J. Alloys and Compd.*, 2011, **509**, 5773-5776.
- 36 N.G. Akdogan, G.C. Hadjipanayis, D.J. Sellmyer, *IEEE Trans. Magn.*, 2009, **45**, 4417-4419.
- 37 J.J. Zhang, H.M. Gao, Y. Yan, X. Bai, F. Su, W.Q. Wang, X.B. Du, *J. Magn. Magn. Mater.*, 2012, **324**, 3272-3275.
- 38 N.G. Akdogan, W. Li, G.C. Hadjipanayis, *J. Nanopart. Res.*, 2012, **14**, 719.
- 39 P.H. Zhou, L.J. Deng, J.L. Xie, D.F. Liang, *J. Alloys Compd.*, 2008, **448**, 303-307.
- 40 S.T. Kao, J.G. Dun, *J. Electron. Mater.*, 2004, **33**, 1445-1451.
- 41 X. Xiao, Z. Zeng, Z. Zhao, S. Xiao, *Mater. Sci. Eng. A*, 2008, **475**, 166-171.
- 42 N. Poudyal, C-b. Rong, J.P. Liu, *J. Appl. Phys.*, 2011, **109**, 07B526-1-07B526-3.
- 43 K.P. Su, D.L. Tao, J. Wang, D.X. Huo, Y.Q. Cao, Z.W. Liu, Y.J. Zhang, *Int. J. Mater. Res.*, 2014, **105**, 1-5.
- 44 O. Glatter, O. Kratky, Academic Press Inc., London, 1982.
- 45 K. Kamino, T. Kawaguchi, M. Nagakura, *IEEE Trans. Magn.*, 1966, **2**, 506-510.
- 46 N. Singh, V. Mudgil, K. Anand, A.K. Srivastava, R.K. Kotnala, A. Dhar, *J. Alloy and Compd.*, 2015, **633**, 401-407.
- 47 O. Glatter, *J. Appl. Cryst.*, 1977, **10**, 415-421.
- 48 B. Jiang, G.J. Weng, *Int. J. Plast.*, 2004, **20**, 2007-2026.
- 49 H.J. Fecht, *Nanostruct. Mater.*, 1995, **6**, 33-42.
- 50 L. Pareti, F. Boizoni and F. Leccabue, *J. Appl. Phys.* 1986, **59**, 3824-3828.
- 51 D. Hobbs, J. Hafner, *J. Phys.: Condens. Matter*, 2001, **13**, L681-L688.
- 52 G. Herzer, *IEEE Trans. Magn.*, 1990, **26**, 1397-1402.
- 53 B.Z. Cui, K. Han, H. Garmestani, J.H. Su, H.J. Schneider-Muntay, J.P. Liu, *Acta Mater.*, 2005, **53**, 4155-4161.
- 54 J.R. Stewart, R. Cywinski, *J. Phys.: Condens. Matter*, 2009, **21**, 124216.

Table 1 Magnetic properties of Mn-Al and Mn-Al-C nanocrystalline powders processed by mechanical milling.

Composition	Methods employed	M_s (emu/g)	H_c (kOe)	Ref.
$Mn_{55}Al_{45}$	IM + OQ + MM + SPS (1393 and 1523 K)	-	1.5	10
$Mn_{54}Al_{46}$	GA + MS + MM + HT (773 K/30 min)	59.8	3.62	11
$Mn_{54}Al_{44}C_2$	IM + MS + IA	0.7*	3.01	15
$Mn_{55-x}Al_{45}C_x$ ($x = 0, 1, 1.7$ and 2); $Mn_{53.5}Al_{45}B_{1.5}$ and $Mn_{52.3}Al_{45}RE_1$ (RE = Pr or Db)	MS + HT (923 K/10 min)	-	1.54	16
$Mn_{70.7}Al_{28.2}C_{1.1}$	MM+CIP+HT (1323 K/10min) + IA (873 K/10 min)	44 [#]	3.4	20
$Mn_{54}Al_{43}C_3$	MS + HT(773 K/10 min)	49	4.1	21
$Mn_{46}Al_{54}$	GA + MM + HT (698 K/45 min)	40	4.4	22
$Mn_{56}Al_{44}$ +5% Fe	MM + SPS + HT (1123 K/20 min)	40.3	2.3	23
$(Mn_{0.54}Al_{0.46})_{100-x}La_x$ $(Mn_{0.535}Al_{0.448}C_{0.017})_{100-x}$ La_x (x up to 0.9)	IM + IA (1373 K) + HT (723 – 873 K)	-	2.5	24
$Mn_{52}Al_{42}C_6$	MM + IA (1323 K) + HT (773 – 973 K/10–60 min)	52	2.6	25
$Mn_{0.53}Al_{0.47-x}C_x$ ($x = 0 - 0.015$)	MM + HT (1173 K/60 min)	72	1.9	26
$Mn_{56}Al_{44}$	MM + SPS + RTP (1123 K/20 min)	28	2.4	27
$Mn_{54}Al_{46}$, $Mn_{54}Al_{43}Cu_3$, $Mn_{54}Al_{40}Cu_6$, $Mn_{54}Al_{37}Cu_9$	MM + HT (693 K)	70	-	28
$Mn_{0.53}Al_{0.47-x}C_x$	MM + HT (1073 K)	81	2.2	29
$Mn_{54}Al_{46}$	SA-HEBM	24.7	4.9	This work

* Tesla, [#] kA/m.

CIP: Cold-isostatic pressing; GA: Gas atomization; MM: Mechanical milling; MS: Melt spinning; HT: Heat treatment; IA: Isothermal aging; IM: Induction melting; OQ: Oil quenching; RTP: Rapid thermal annealing; SA-HEBM: Surfactant-assisted High Energy Ball Milling; SPS: Spark plasma sintering.

Table 2 Characteristics of Mn-Al powders processed by HEBM and SA-HEBM processes.

Milling duration (h)	Mean grain size by XRD (nm)		Flakes obtained by SA-HEBM	
	HEBM	SA-HEBM	Thickness (nm)	Length (μm)
2	22.5	20.5	1000 - 3000	1 - 45
4	20.7	19.4	500 - 950	1 - 60
6	19.6	17.6	150 - 300	1 - 74
8	19.3	15.8	90 - 160	1 - 90
10	19.1	15.5	75 - 150	1 - 90



Fig.1 Photograph showing the formation of Mn-Al colloidal nanoparticles (suspension) in the case of 8-h milled Mn-Al powders with OA+OY (a), which is compared with that of those prepared without OA+OY (b).

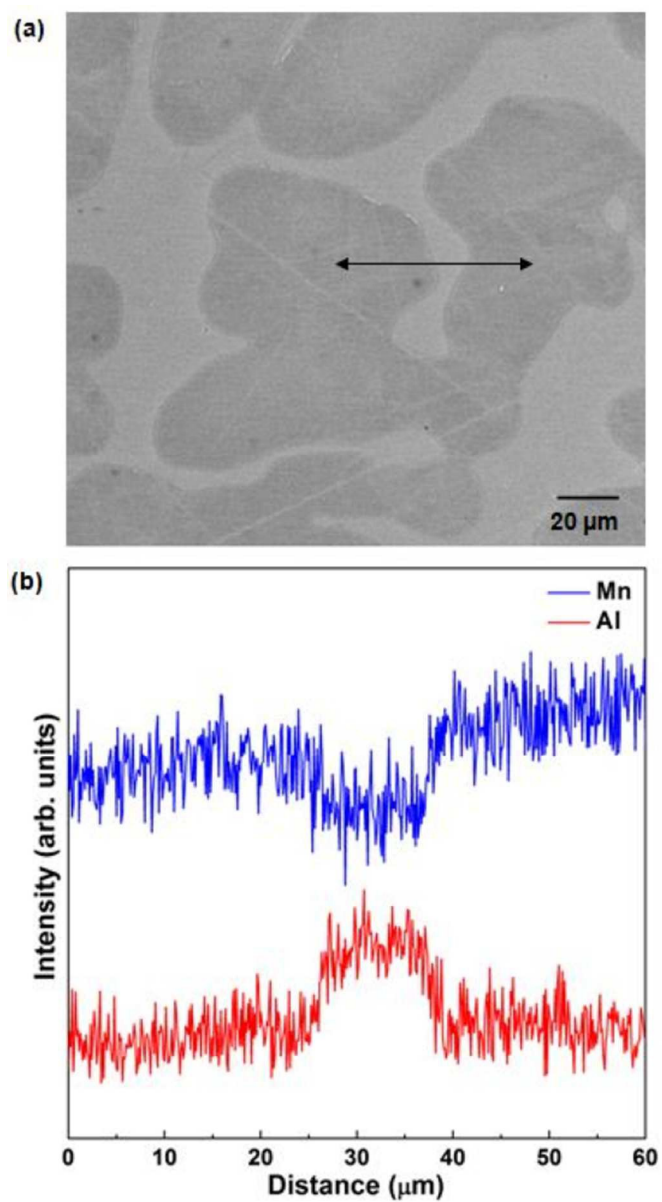


Fig.2 SEM back-scattered electron micrograph showing two-phase morphology for the as-cast Mn-Al alloy with the solid line marks the region for EDS line scan (a) and its corresponding EDS profile (b).

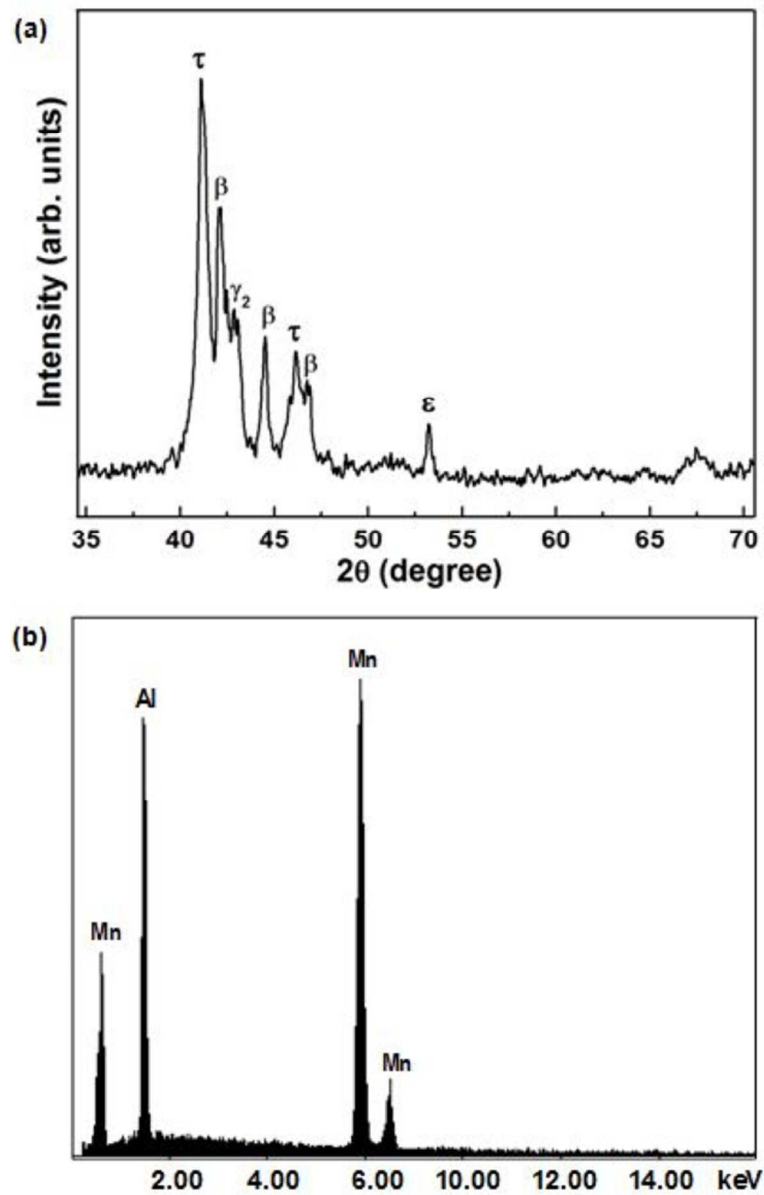


Fig.3 Typical XRD pattern (a) and EDS spectrum (b) of as-cast Mn-Al alloy processed by arc-melting.

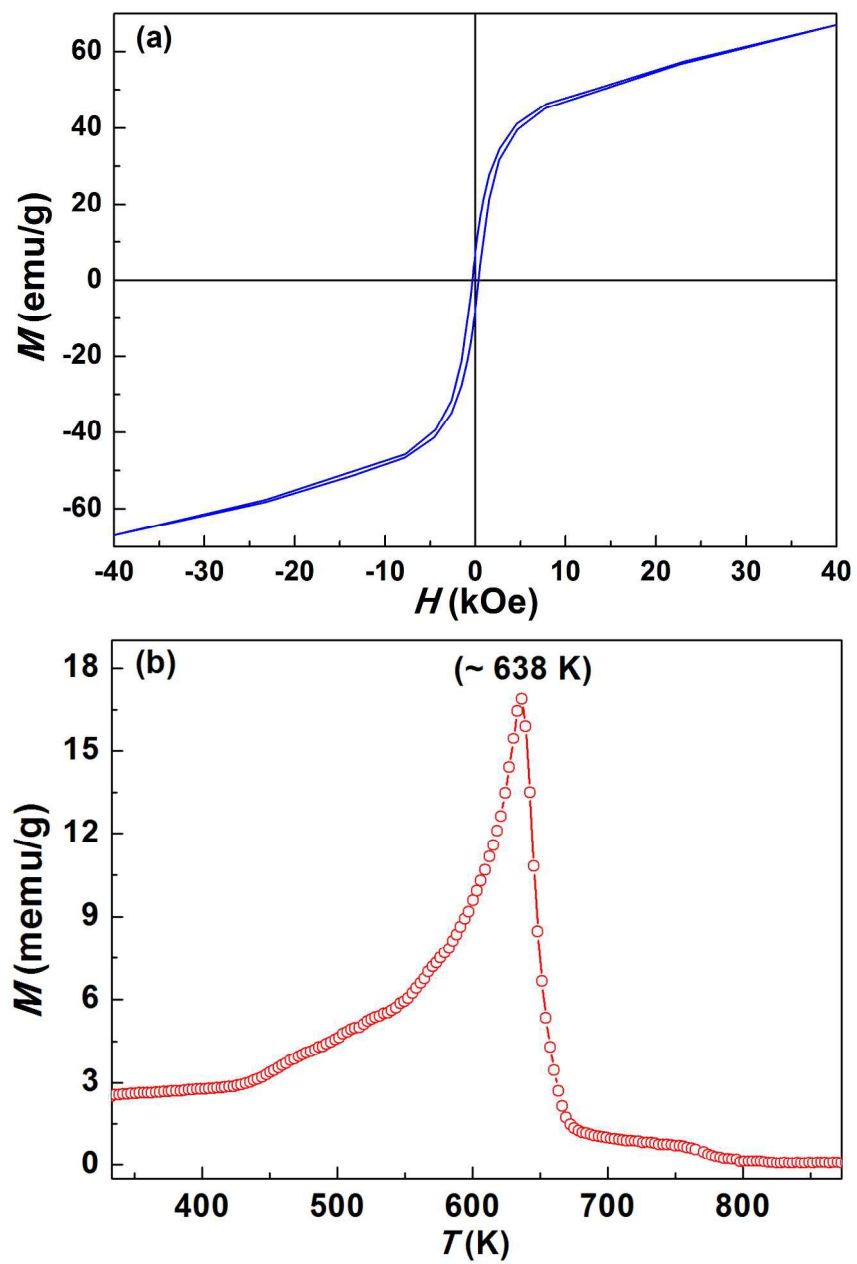


Fig.4 $M-H$ (a) and $M-T$ (b) curves for the as-cast Mn-Al alloy ingot.

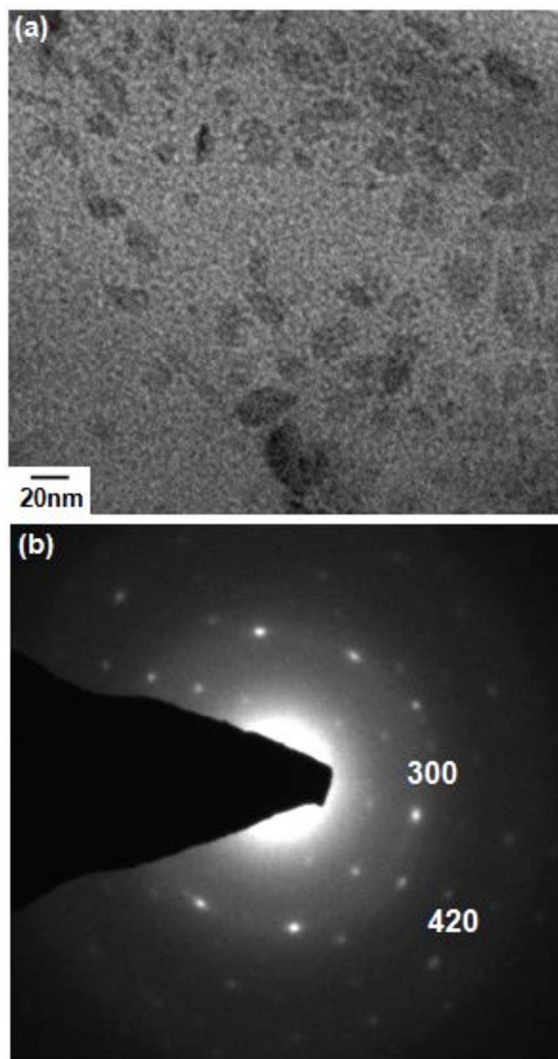


Fig.5 TEM micrograph of the Mn-Al colloidal nanoparticles obtained after 8-h of SA-HEBM process (a) and its corresponding SAED pattern (b).

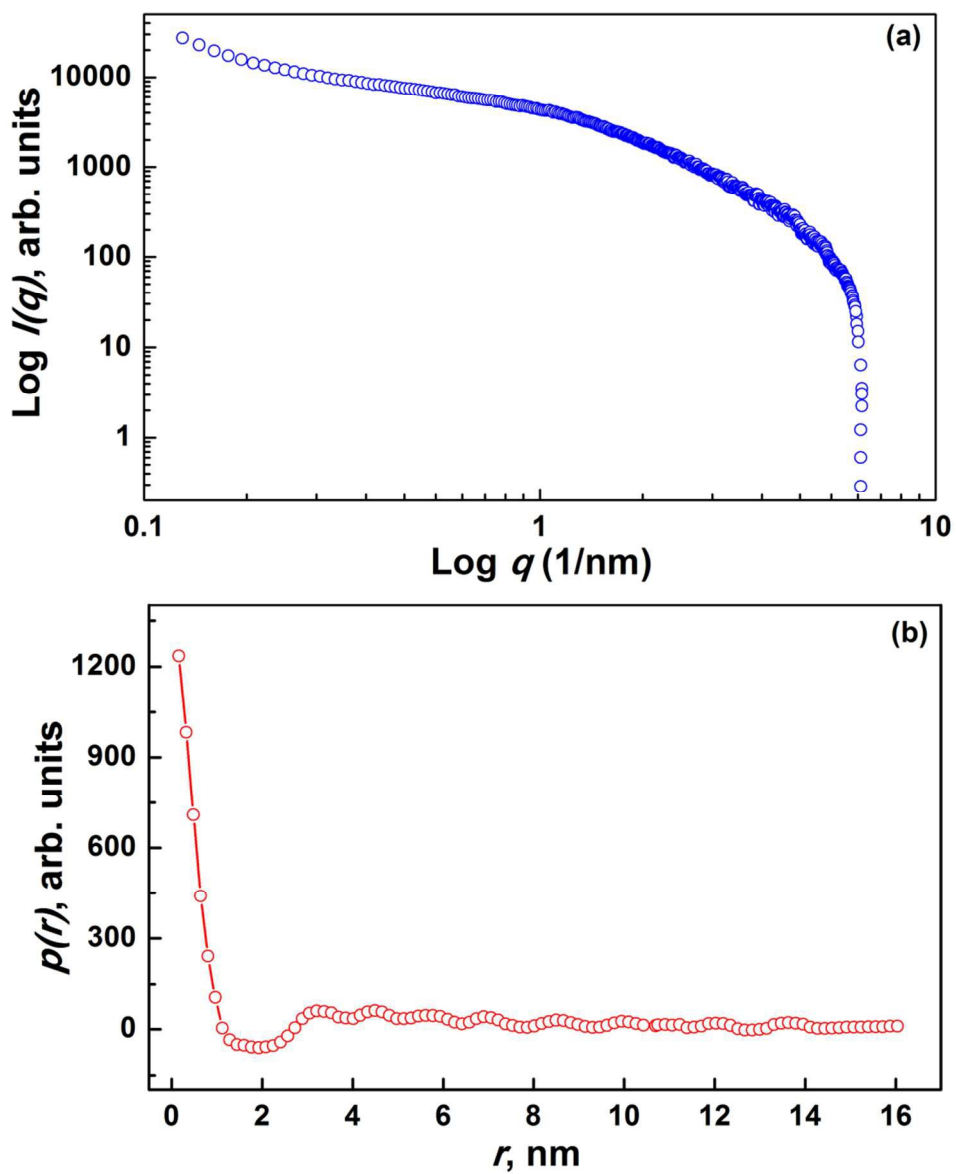


Fig.6 Plots of the experimental scattering intensity, $\log I(q)$ versus the scattering vector $\log q$ (a) and the experimental pair distance distribution function $p(r)$ versus radial distance r (b) for the Mn-Al colloid processed by SA-HEBM.

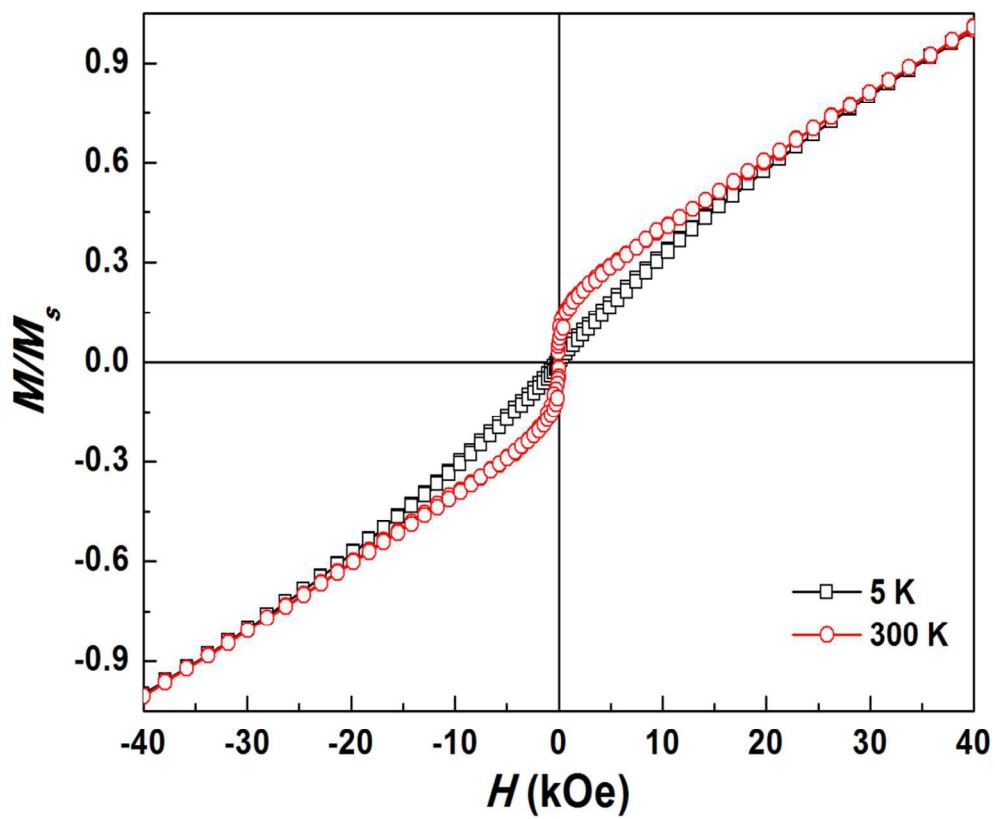


Fig.7 $M-H$ loops of Mn-Al colloids obtained at 300 and 5 K with their magnetic moment is normalized for maximum saturation value.

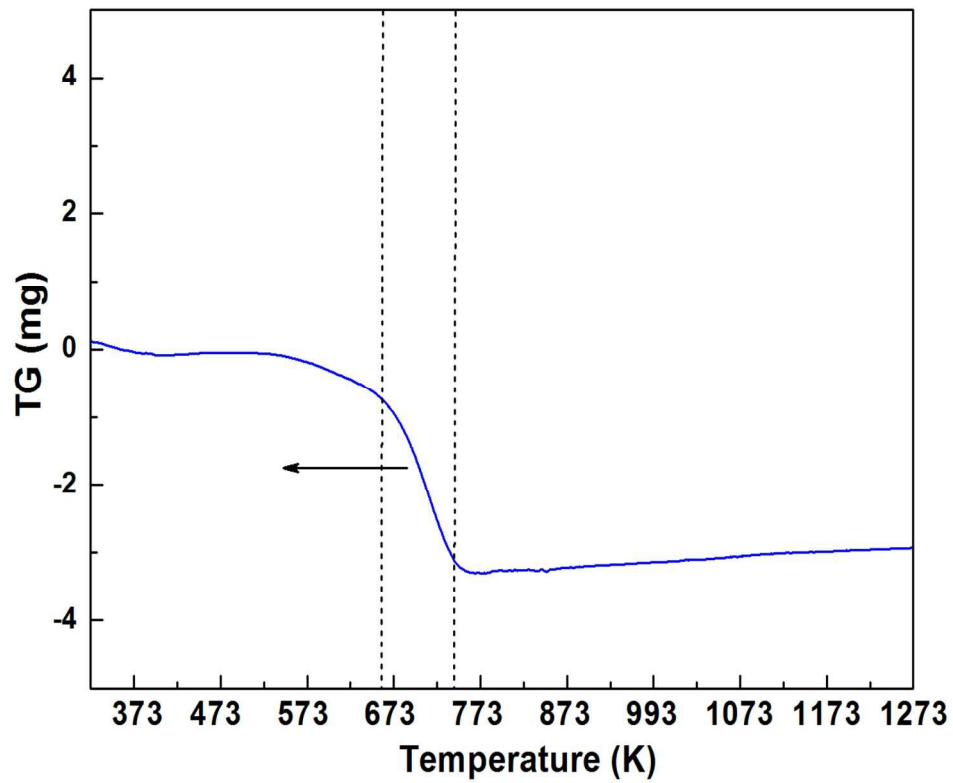


Fig.8 Typical TG curve for the 8-h milled Mn-Al powders with OA+OY.

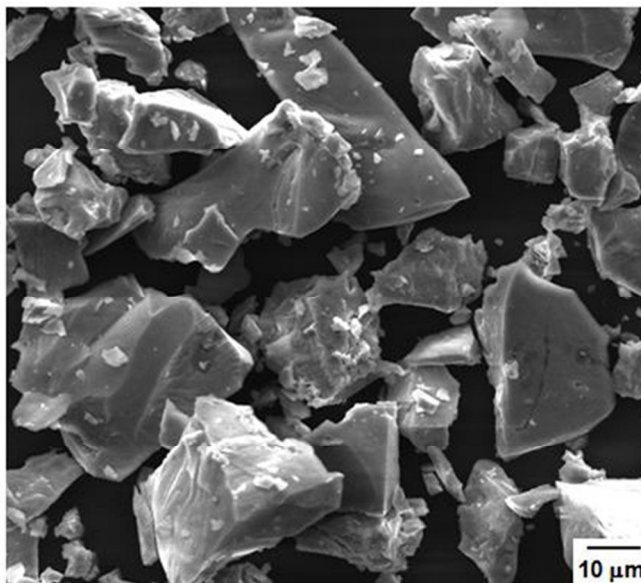


Fig.9 SEM micrograph of as-cast Mn-Al alloy after crushing.

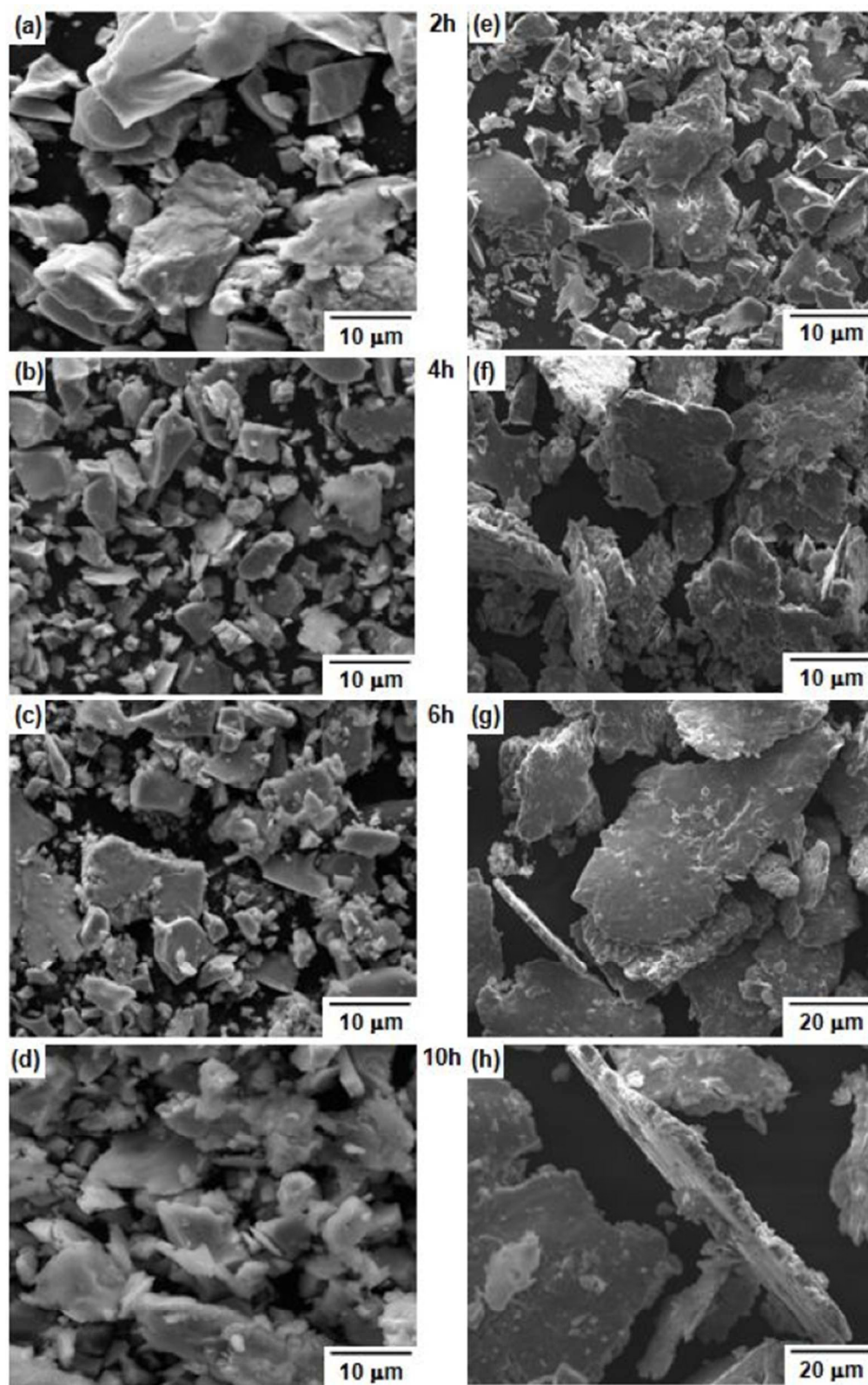


Fig.10 SEM micrographs of Mn-Al powders obtained at different milling duration without (a–d) and with OA+OY (e–h).

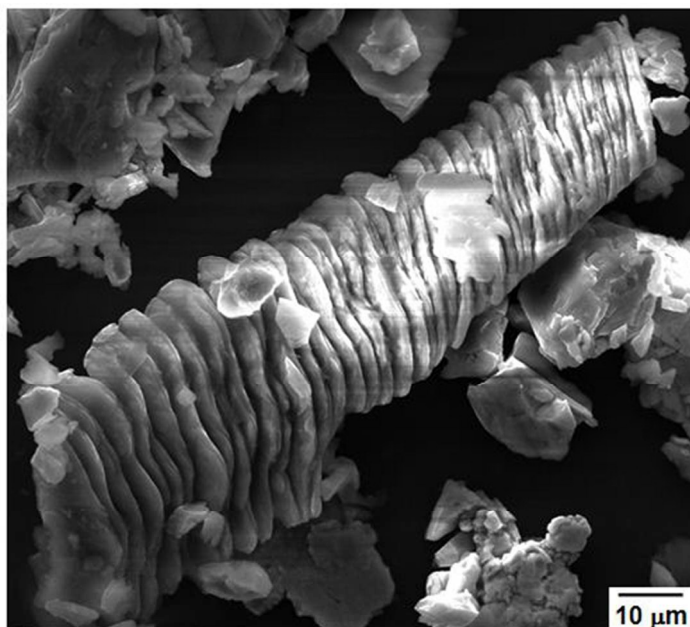


Fig.11 Development of nanocrystalline flake-like structure during SA-HEBM process of Mn-Al powders after 2 h of milling.

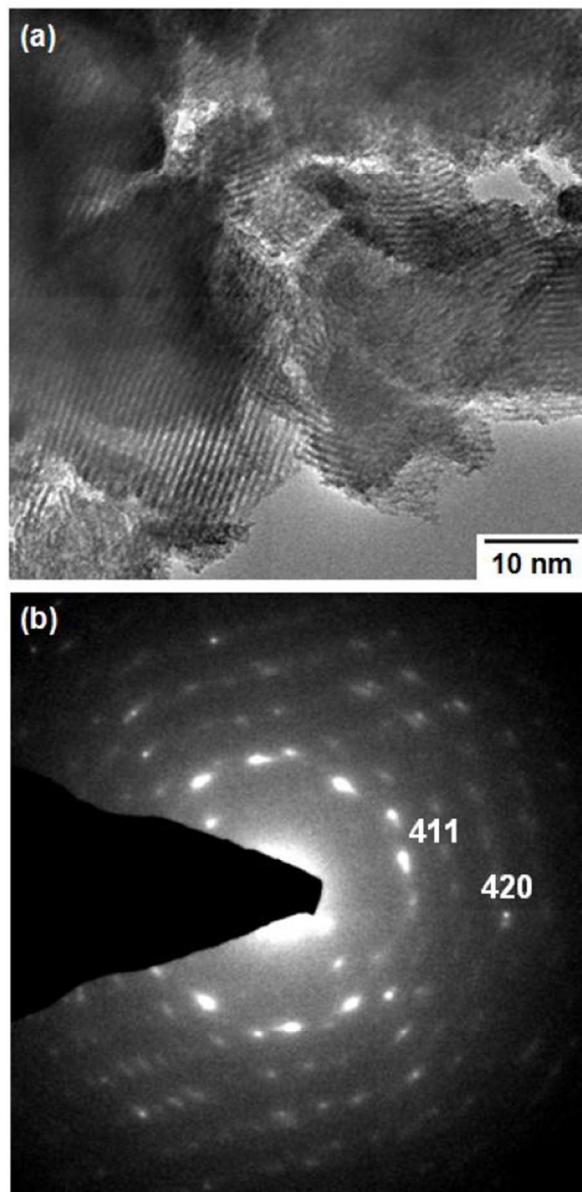


Fig.12 HRTEM micrograph of nanocrystalline Mn-Al flakes obtained after 8-h of SA-HEBM process (a) and the corresponding SAED pattern (b).

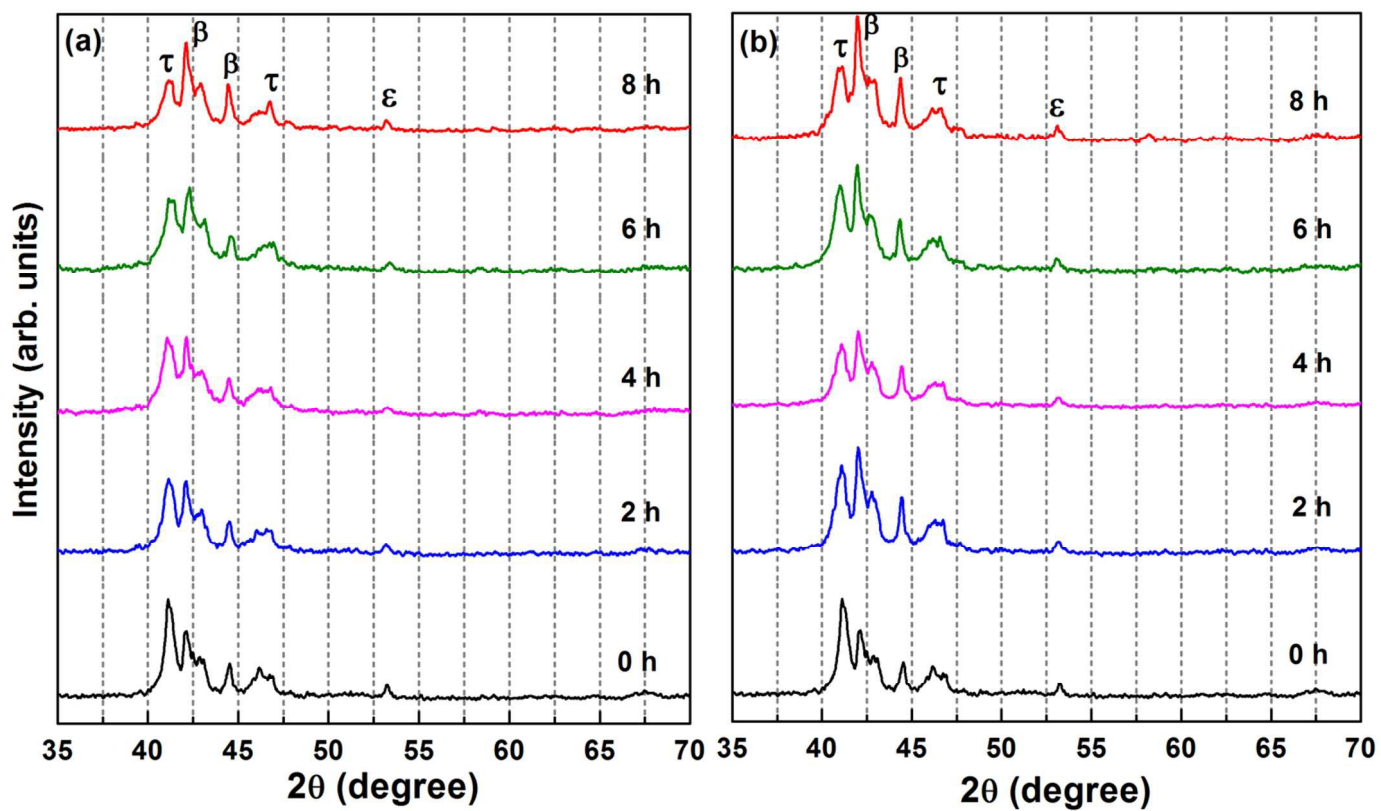


Fig.13 XRD patterns obtained for the Mn-Al powders as a function of milling time: without (a) and with OA+OY (b).

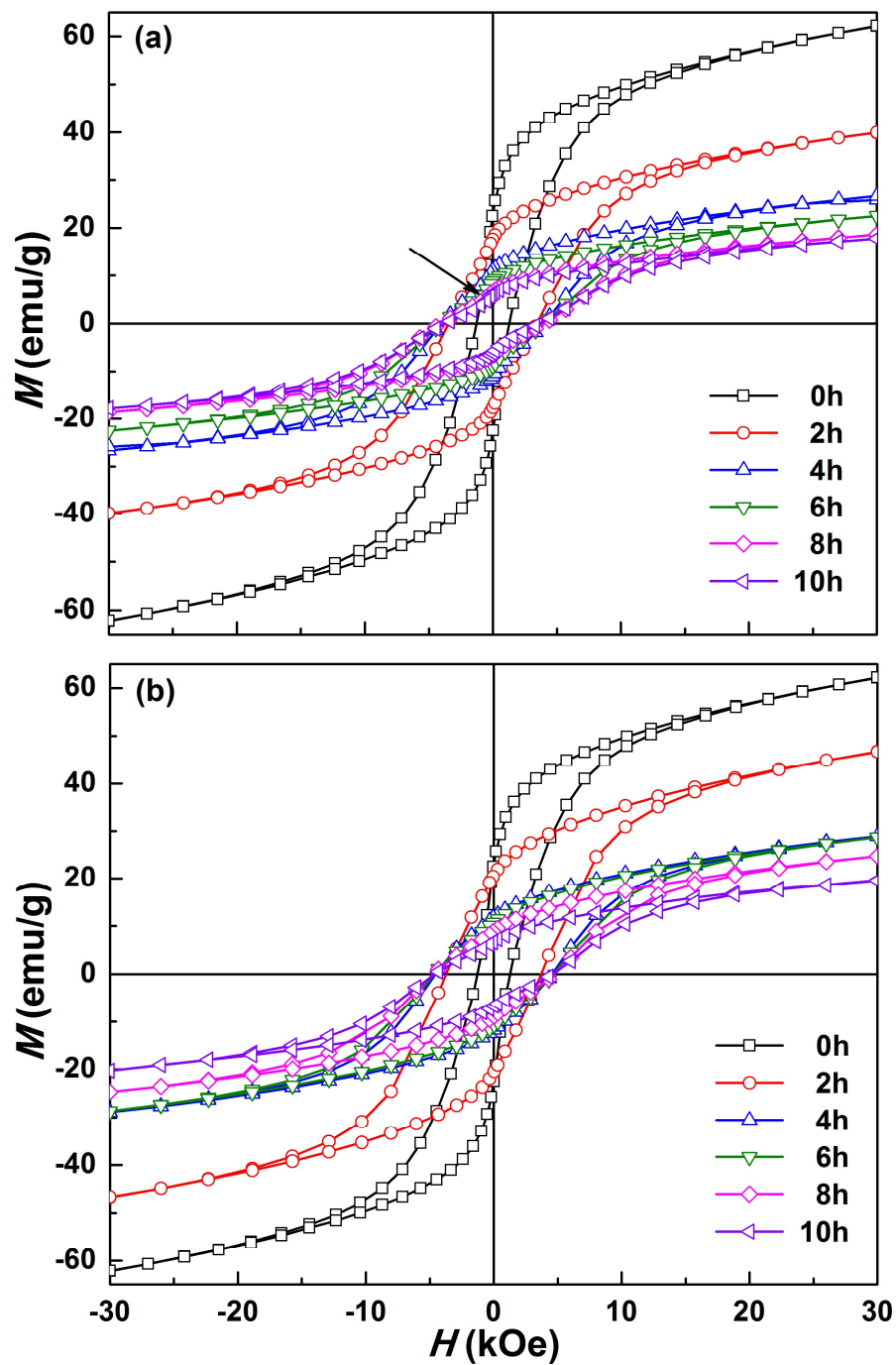


Fig.14 Room temperature magnetic hysteresis curves for the Mn-Al powders obtained at different milling intervals without (a) and with OA+OY (b).

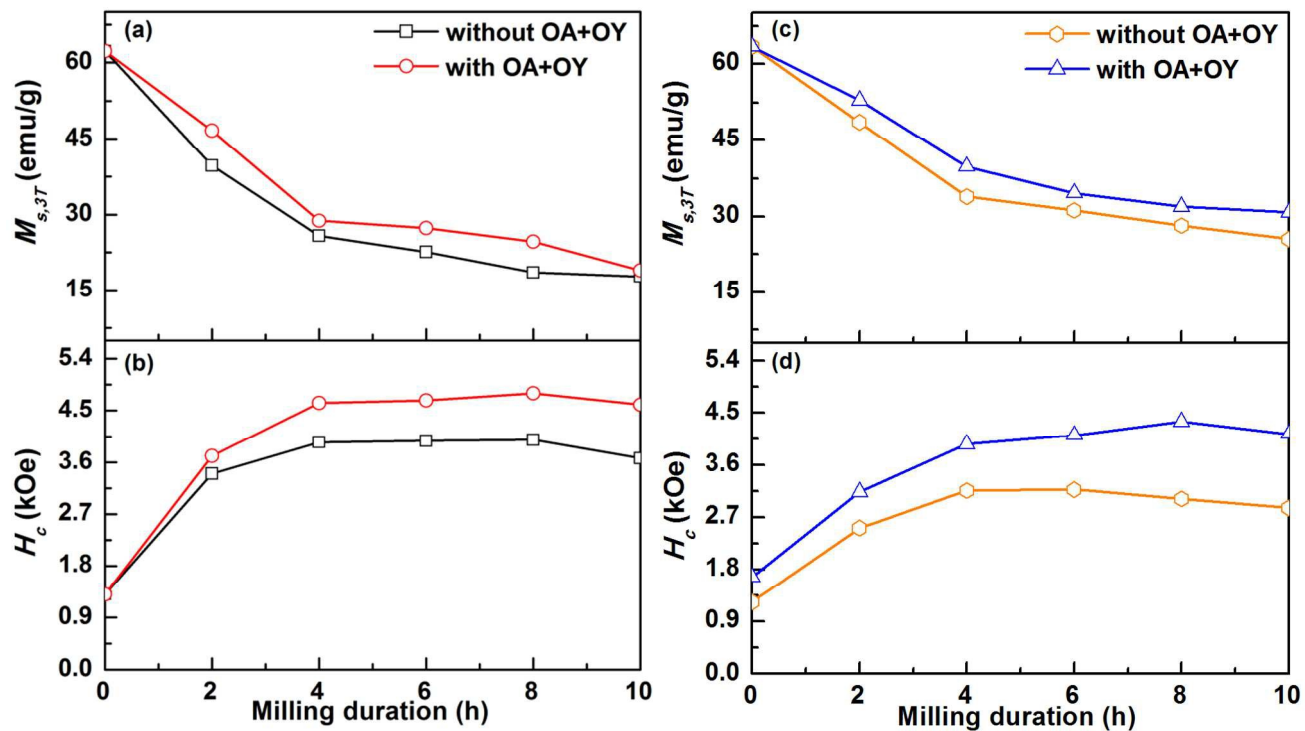


Fig.15 M_s and H_c values as a function of milling duration for the Mn-Al powders processed with and without OA+OY. (a-b) as-milled and (c-d) after being annealed at 623 K / 10 min.

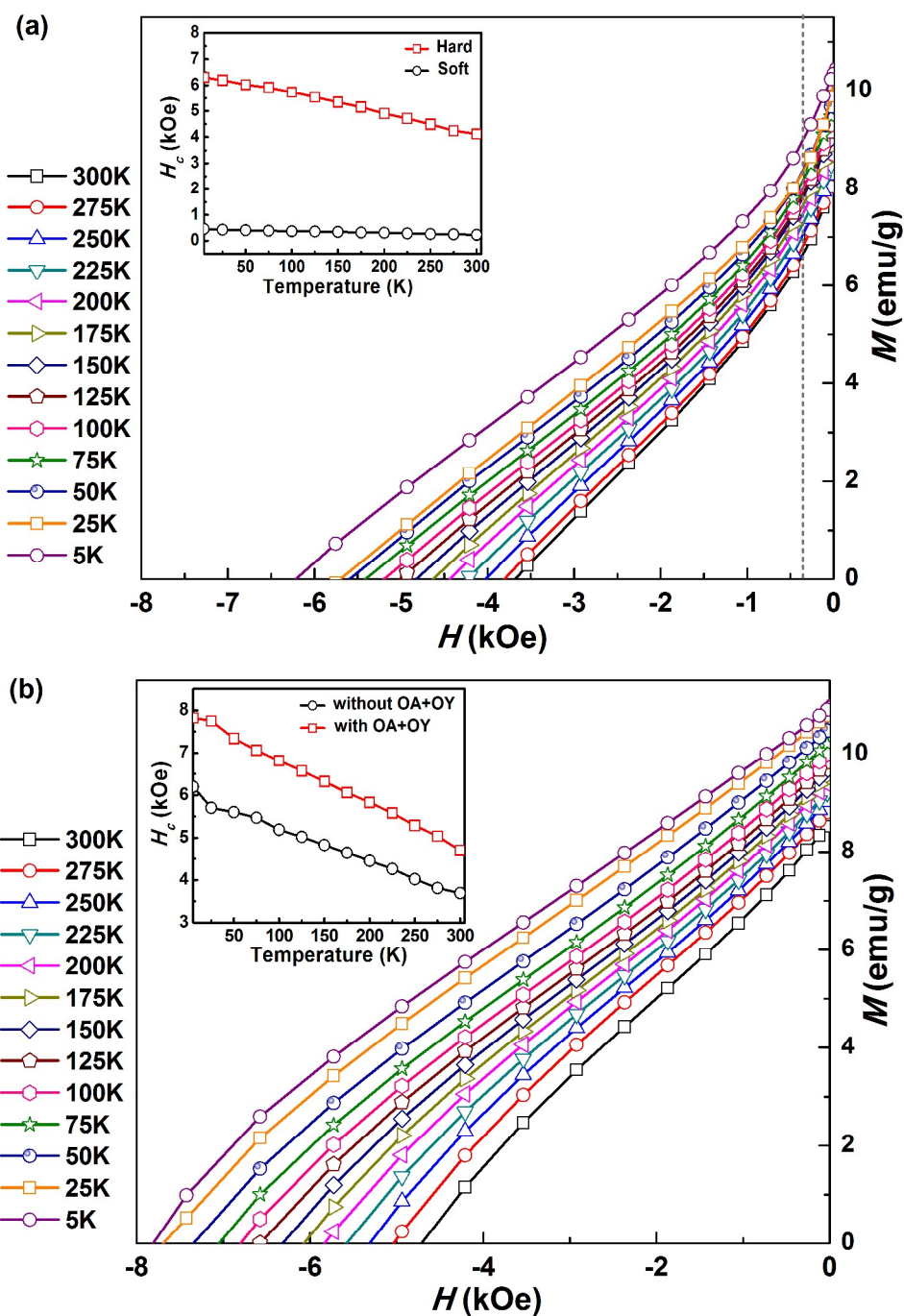


Fig.16 Temperature dependence 2nd quadrant demagnetization curves for the 8-h milled Mn-Al powders without (a) and with OA+OY. Inset of (a): Temperature dependence of H_c of hard and soft phases present in the 8-h milled Mn-Al powder processed without OA+OY. Inset of (b): H_c as a function of temperature for the 8-h milled Mn-Al powders without and with OA+OY.